

Yong Du^a, Y. A. Chang^b, Shuhong Liu^a, Baiyun Huang^a, F.-Y. Xie^b, Ying Yang^b, S.-L. Chen^b

^aState Key Laboratory of Powder Metallurgy, Central South University, Hunan, P.R. China

^bDepartment of Materials Science and Engineering, University of Wisconsin-Madison, Madison, USA

Thermodynamic description of the Al–Fe–Mg–Mn–Si system and investigation of microstructure and microsegregation during directional solidification of an Al–Fe–Mg–Mn–Si alloy

The thermodynamic database for the Al–Fe–Mg–Mn–Si system is developed based on the constituent binary, ternary, and quaternary systems. The computed phase diagrams agree well with the experimental data. The obtained database is used to describe the solidification behavior of Al 356.1 (91.95Al–0.46Fe–0.3Mg–0.32Mn–6.97Si, in wt.%) and Al 356.2 (92.77Al–0.08Fe–0.35Mg–6.8Si, in wt.%) under equilibrium and Gulliver–Scheil non-equilibrium conditions. The reliability of the established thermodynamic database is also verified by the good agreement between calculation and experiment for both equilibrium and Gulliver–Scheil non-equilibrium solidifications. Microstructure and microsegregation of the directionally solidified Al 356.1 alloy are investigated with a growth rate of $0.04445 \text{ cm s}^{-1}$ and a temperature gradient of 45 K cm^{-1} . Fractions of solids formed are measured by using quantitative image analysis of back-scattered electron, and solute redistribution in the primary (Al) is determined by means of an area scan approach with a total of 2400 electron probe microanalysis point counts. A micromodel, which includes solid-state diffusion, secondary dendrite arm coarsening, and dendrite tip and eutectic undercooling, is coupled with a multicomponent phase diagram calculation engine (PanEngine) to predict the microstructure and microsegregation of the solidified alloy. Quantitative agreement of the model prediction with the experiment is obtained for concentration distributions in the primary (Al), the types and amounts of phases formed, and the solidification path.

Keywords: Microstructure; Microsegregation; Electron probe microanalysis; Directional solidification; Micromodel; Al alloys

1. Introduction

Accurate predictions of microstructure (i.e., types and amounts of phases formed and dendrite arm spacings) and

microsegregation (i.e., redistribution of alloy elements between the dendrites) during solidification are of prime importance. The mechanical and chemical properties as well as the corrosion resistance of solidified alloys are heavily dependent on the microstructure and microsegregation obtained after solidification [1]. Information on microstructure and microsegregation is essential to design solidification process and subsequent heat treatments in order to obtain optimal material properties. Although numerous publications, both theoretical and experimental investigations, are available on microstructure and microsegregation in binary alloys, as summarized in the reviews [2–6], there are only limited comprehensive studies of solidification for multicomponent alloys [7–11], especially with respect to the solute redistribution in the solidified microstructure. Consequently, there is a strong industrial need to remedy this situation since nearly all the current commercial alloys contain many components, often exceeding ten elements.

In order to predict microstructure and microsegregation of multicomponent alloys accurately, the main thermodynamic (including phase diagrams) and kinetic data (diffusion coefficients, solid/liquid interfacial energies, specific latent heats of solidification, geometric factors for dendrite coarsening, etc.) are needed.

The aim of the present work is to investigate the microstructure and microsegregation in a directionally solidified Al 356.1 alloy (91.95Al–0.46Fe–0.3Mg–0.32Mn–6.97Si, in wt.%) via both experiment and modeling. The thermodynamic database for the quinary Al–Fe–Mg–Mn–Si system is first established on the basis of the constituent binary, ternary, and quaternary systems. The experimental procedures for the equilibrium solidification and directional solidification of Al 356.1 alloy are then presented, followed by a brief description of the thermodynamic and microsegregation models. The last part is devoted to the comparison between experiment and calculation for phase diagram, solute redistributions in the primary (Al), the phases formed and their amounts, and the solidification path.

2. Thermodynamic database for the Al–Fe–Mg–Mn–Si system

2.1. The binary systems

There are 10 binary systems in the quinary system. The thermodynamic parameters for these binary systems are taken from COST 507 project [12].

2.2. The ternary systems

The thermodynamic data sets for the Al–Mg–Si and Al–Mn–Si systems published in COST 507 project [12] are accepted in the present work. The thermodynamic parameters for the Al–Fe–Si, Fe–Mn–Si, and Fe–Mg–Si systems are taken from Liu and Chang [13], Forsberg and Ågren [14], and Daniel [15], respectively.

The thermodynamic parameters for the Al–Fe–Mn and Al–Mg–Mn systems have been reported [12]. However, the published parameters cannot describe the experimental phase equilibria in the Al-rich regions of the ternary systems [16, 17]. In the present work, the thermodynamic parameters for the liquid phase in the above two ternary systems are assessed in order to reproduce the experimentally measured phase equilibria [16, 17]. The thermodynamic parameter for the liquid phase in the Al–Fe–Mg system is assessed to describe the phase equilibria in the Al-rich part of the system [16]. The remaining two ternary systems Fe–Mg–Mn and Mg–Mn–Si are assumed to behave as ideal solutions, i. e. their thermodynamic parameters are synthesized from the corresponding sub-binary sides.

2.3. The quaternary systems

2.3.1. The Al–Fe–Mg–Si system

Using thermal analysis (TA) and optical microscopy, Phillips [18] investigated the phase equilibria on the Al-rich side of the Al–Fe–Mg–Si system in the composition ranges of 0 to 12 wt.% Mg, 0 to 14 wt.% Si, and 0 to 2.5 wt.% Fe. On the basis of TA and chemical analysis, Gul'din and Dokukina [19] measured the solubility of Fe and Si in Al–Mg melts and the eutectic reaction temperature for $L = (Al) + Mg_2Si + Al_{13}Fe_4 + Al_8Mg_5$. The quaternary phase π ($Al_{16}Fe_2Mg_6Si_{12}$) found by Phillips [18] was shown to have the composition $Al_{18}Fe_2Mg_7Si_{10}$ by Krendelsberger et al. [20] using single crystal automatic four circle counter data. Most recently, Daniel [15] has modeled this quaternary system. However, the calculated liquidus compositions in the invariant equilibria show noticeable discrepancies (up to 10 at.%) from the experimental ones. A reassessment of this quaternary system is necessary in order to provide a reliable basis for thermodynamic calculations in related multi-component systems.

2.3.2. The Al–Fe–Mn–Si system

The phase equilibria on the Al-rich side of the quaternary Al–Fe–Mn–Si system have been the subject of numerous investigations [21–31]. By means of TA and metallographic examination methods, Phillips and Varley [21] obtained the liquidus surface, the solidus surface, and 16 isopleths over the composition ranges of 0 to 4 wt.% Fe, 0 to

4 wt.% Mn, and 0 to 4 wt.% Si. They found the existence of the ternary phases α -AlFeSi (Al_8Fe_2Si), β -AlFeSi (Al_5FeSi), and α -AlMnSi ($Al_{15}Mn_3Si_2$). α -AlMnSi and α -AlFeSi form a continuous series of solid solution [21]. Although the pioneering work by Phillips and Varley is emphasized in the literature, the published phase relations [21] are considered to be only approximate because (i) the liquidus temperatures measured by them [21] are substantially too low (at least 20 °C), as pointed out by Du et al. in the investigation of the Al–Mn–Si system [32] and (ii) true equilibrium is not reached in their experiment as five phases are observed in wide temperature and composition ranges at the presented isopleths.

Employing X-ray diffraction (XRD) and metallographic observation techniques, Nowotny and Marquardt [22] measured the 500 °C isothermal section of the Al–Fe–Mn–Si system at 88 wt.% Al and below 12 wt.% Fe and 12 wt.% Mn. The isothermal section presented by them [22] is based on imperfect ternaries and is, therefore, of limited value. Phragmen [23] found a quaternary phase with the composition α -Al(Fe, Mn)Si. The existence of this quaternary phase was confirmed by Barlock and Mondolfo [24], who suggested the stoichiometry $Al_{15}(Fe, Mn)_3Si_2$ using XRD technique.

The six isopleths (at 10 wt.% Si with 1 wt.% Fe or 2 wt.% Fe or 3 wt.% Fe, and at 14 wt.% Si with 1 wt.% Fe or 2 wt.% Fe or 3 wt.% Fe) below 4 wt.% Mn were constructed by Zakharov et al. [25, 26] using differential thermal analysis (DTA), optical microscopy, and XRD techniques. In the presented isopleths, the phase boundaries are based on the cooling curves with cooling rates of 2 to 3 K min^{−1}. In addition to the isopleths, Zakharov et al. [25, 26] reported the existence of a quaternary phase with a stoichiometry $Al_{16}(Fe, Mn)_4Si_3$. They also found that either α -AlFeSi or β -AlFeSi and α -AlMnSi do not form continuous solid solutions owing to the different crystal structures. It was reported that β -AlFeSi and α -AlMnSi dissolve less than 0.5 at.% Mn and less than 1 at.% Fe, respectively. Thoresen et al. [27] and Simensen et al. [28, 29] confirmed that α -AlFeSi dissolves a small amount of Mn (up to 0.5 at.%). Using DTA technique, Flores–Valdes et al. [30] reported that the melting temperature corresponding to the stoichiometry $Al_8FeMnSi_2$ is 795 °C. It is not clear if the quaternary phase is formed congruently or via a peritectic reaction since neither XRD pattern nor microstructure is presented [30].

The key contributions to the understanding of the phase equilibria in the Al-rich corner of the Al–Fe–Mn–Si system are the work by Davignon et al. [31], who analyzed 19 quaternary alloys using optical microscopy and electron probe microanalysis (EPMA). Confirming the previous investigations [21, 24–26], Davignon et al. [31] found that β -AlFeSi dissolves about 0.5 at.% Mn at 550 °C. In contradiction to the previously mentioned authors [21, 24–26], they [31] claimed that the solubility of Fe in α -AlMnSi is up to 12 at.% at 550 °C. As will be mentioned later, the present experiment confirms the findings of Davignon et al. [31].

Using the equilibrium constant for the reaction leading to the formation of the quaternary phase $Al_8FeMnSi_2$, Flores–Valdes et al. [33] derived the Gibbs energy of formation for this quaternary phase. On the basis of energy-dispersive X-ray (EDX) microprobe analysis of the precipitated solid phases, Onderka et al. [34] found the existence

of another quaternary phase $\text{Al}_{11.8}\text{FeMn}_{1.6}\text{Si}_{1.6}$. This quaternary phase is not included in the thermodynamic optimization since there is no experimental information on its equilibrium with any other phases.

Most recently, Balitchev et al. [35] performed a thermodynamic assessment of the quaternary Al–Fe–Mn–Si system using the experimental data mainly published by Zakharov et al. [25, 26]. The large solid solubility of Fe in $\alpha\text{-AlMnSi}$ [31] as well as the melting behavior [30] of the quaternary phase $\text{Al}_8\text{FeMnSi}_2$ are not considered in the modeling of Balitchev et al. [35].

In the present work, the thermodynamic parameters for the phases $\text{Al}_8\text{FeMnSi}_2$, $\alpha\text{-AlMnSi}$, and $\beta\text{-AlFeSi}$ are evaluated by considering the invariant reaction data [21, 25, 26], the melting temperature of the quaternary phase $\text{Al}_8\text{FeMnSi}_2$ [30], and the phase assemblage data [31].

2.3.3. The Al–Fe–Mg–Mn, Al–Mg–Mn–Si, and Fe–Mg–Mn–Si systems

No quaternary phases were found in the Al–Fe–Mg–Mn and Al–Mg–Mn–Si quaternary systems [23]. In the literature, there is no experimental information on the phase equilibrium in the Fe–Mg–Mn–Si quaternary system. As a consequence, the thermodynamic properties for the above three quaternary systems are synthesized from the descriptions of the constituent ternary systems.

2.4. The Al–Fe–Mg–Mn–Si quinary system

Using TA and microstructure observation techniques, Barlock and Mondolfo [24] found that the eutectic reaction $L = (\text{Al}) + \text{Al}_3\text{Fe} + \text{Al}_8\text{Mg}_5 + \text{Mg}_2\text{Si} + \text{Al}_8\text{Mg}_2\text{Mn}_2$ occurs at 445 °C.

3. Experimental procedure

In order to compare the equilibrium solidification characteristics calculated by using the established thermodynamic database with the experimental measurement, the as-cast Al 356.1 sample is annealed at 500 °C for 45 days under high vacuum in a quartz tube (10^{-4} bar). The water-quenched sample is then subjected to differential scanning calorimetry (DSC) measurement (Perkin-Elmer model II, Norwalk, Connecticut, USA) with a heating and cooling rate of 5 K min⁻¹.

Since the directional solidification apparatus utilized in the present work was described elsewhere [36] in detail, only its brief description is given here. A rod-like Al 356.1 sample, 3 mm in diameter and 20 cm in length, was sealed in a high-purity alumina tube and then heated in a temperature gradient furnace, which consists of a vertical furnace with an attached cooling device. The specimen can be moved with varying speeds, while the furnace was spatially fixed. The Al 356.1 specimens were superheated to about 100 °C above the liquidus temperature for 2 h prior to the start of directional solidification. The sample was solidified to about 10 to 15 cm with a growth rate of 0.04445 cm s⁻¹ and a temperature gradient of 45 °C cm⁻¹ near the solid/liquid interface. After the solidification, the sample was quenched in a water-ice mixture. The transverse sections were ground and then polished to 0.25 μm. The solidified microstructure was analyzed by means of optical micro-

scopy and EPMA (CAMECA SX-50, France) techniques. The composition measurements were performed using a wavelength-dispersive spectrum (WDS) method. Al, Fe, Si, MgO, and NiMn were used as the standards of Al, Fe, Si, Mg, and Mn, respectively. A total of 400 measurements were carried out automatically over an area of 800 × 800 μm² of a transverse section. Totally 2400 measurements were conducted on six transverse sections. The volume fractions of the solidified phases were measured by automatic image analysis of the back-scattered electron (BSE) images.

4. Thermodynamic and microsegregation models

4.1. Thermodynamic model

The quaternary phase $\text{Al}_8\text{FeMnSi}_2$, which is shown to have the stoichiometry $\text{Al}_{16}\text{Fe}_2\text{Mn}_2\text{Si}_3$ [25, 26], is treated as a stoichiometric phase, and its Gibbs energy is expressed relative to the mechanical mixing of the pure elements by the following equation:

$$G_{\text{m}}^{\text{Al}_{16}\text{Fe}_2\text{Mn}_2\text{Si}_3} - H^{\text{SER}} = 16 \cdot {}^{\circ}G_{\text{Al}}^{\text{fcc}-\text{Al}} + 2 \cdot {}^{\circ}G_{\text{Fe}}^{\text{bcc}-\text{A2}} + 2 \cdot {}^{\circ}G_{\text{Mn}}^{\text{cbcc}-\text{A12}} + 3 \cdot {}^{\circ}G_{\text{Si}}^{\text{dia}} + A + BT \quad (1)$$

in which the coefficients A and B are assessed from the experimental phase diagram data. The Gibbs energy of the phase $\text{Al}_{18}\text{Fe}_2\text{Mg}_7\text{Si}_{10}$ is defined in a fashion similar to Eq. (1).

In view of the large solubility for Fe in $\alpha\text{-AlMnSi}$, this phase is described with the sublattice model $\text{Al}_{16}(\text{Fe}, \text{Mn})_4\text{Si}_1(\text{Al}, \text{Si})_2$. In order to reduce the number of adjustable parameters, it is assumed that Fe only substitutes for Mn in the second sublattice. According to the formula for sublattice model [37, 38], the Gibbs energy of $\text{Al}_{16}(\text{Fe}, \text{Mn})_4\text{Si}_1(\text{Al}, \text{Si})_2$ per mole-formula can be expressed as:

$$\begin{aligned} {}^{\circ}G^{\alpha\text{-AlMnSi}} - H^{\text{SER}} = & y'_{\text{Fe}} \cdot y''_{\text{Al}} \cdot {}^{\circ}G_{\text{Al:Fe:Si:Al}}^{\alpha\text{-AlMnSi}} \\ & + y'_{\text{Fe}} \cdot y''_{\text{Si}} \cdot {}^{\circ}G_{\text{Al:Fe:Si:Si}}^{\alpha\text{-AlMnSi}} \\ & + y'_{\text{Mn}} \cdot y''_{\text{Al}} \cdot {}^{\circ}G_{\text{Al:Mn:Si:Al}}^{\alpha\text{-AlMnSi}} \\ & + y'_{\text{Mn}} \cdot y''_{\text{Si}} \cdot {}^{\circ}G_{\text{Al:Mn:Si:Si}}^{\alpha\text{-AlMnSi}} \\ & + 4RT (y'_{\text{Fe}} \cdot \ln y'_{\text{Fe}} + y'_{\text{Mn}} \cdot \ln y'_{\text{Mn}}) \\ & + 2RT (y''_{\text{Al}} \cdot \ln y''_{\text{Al}} + y''_{\text{Si}} \cdot \ln y''_{\text{Si}}) \\ & + y'_{\text{Fe}} \cdot y'_{\text{Mn}} \cdot y''_{\text{Al}} \cdot L_{\text{Al:Fe,Mn:Si:Al}}^{\alpha\text{-AlMnSi}} \\ & + y'_{\text{Fe}} \cdot y'_{\text{Mn}} \cdot y''_{\text{Si}} \cdot L_{\text{Al:Fe,Mn:Si:Si}}^{\alpha\text{-AlMnSi}} \\ & + y'_{\text{Fe}} \cdot y'_{\text{Al}} \cdot y''_{\text{Si}} \cdot L_{\text{Al:Fe:Si:Al, Si}}^{\alpha\text{-AlMnSi}} \\ & + y'_{\text{Mn}} \cdot y'_{\text{Al}} \cdot y''_{\text{Si}} \cdot L_{\text{Al:Mn:Si:Al, Si}}^{\alpha\text{-AlMnSi}} + \dots \quad (2) \end{aligned}$$

where the four parameters denoted ${}^{\circ}G_{\text{Al:*,Si:*,*}}^{\alpha\text{-AlMnSi}}$ (also called compound energies) are expressed relative to the Gibbs energies of pure fcc Al, bcc Fe, cbcc Mn, and diamond Si at the same temperature. The superscripts ' and '' mean the second and the last sublattices of the model $\text{Al}_{16}(\text{Fe}, \text{Mn})_4\text{Si}_1(\text{Al}, \text{Si})_2$, respectively.

An equation similar to Eq. (2) can be written for the Gibbs energy of $\beta\text{-AlFeSi}$, which is modeled as $\text{Al}_{0.598}(\text{Fe}, \text{Mn})_{0.152}\text{Si}_{0.1}(\text{Al}, \text{Si})_{0.15}$.

4.2. Microsegregation model

The numerical micromodel [7, 36] for the prediction of the microstructure and microsegregation in multicomponent alloys during dendrite solidification is based on that of Kraft et al. [39]. The model due to Kraft et al. [39] is basically an extension of the modified Gulliver–Scheil model [40, 41] to multicomponent systems incorporating solid–back diffusion, dendrite tip and eutectic undercooling, and dendrite arm coarsening. Three geometric shapes, plate, cylinder, and sphere, are used to describe the growing secondary or tertiary arms.

The solid–back diffusion in the (Al) phase is described by solving the multicomponent form of Fick’s second law via a finite difference method. For the diffusion the (Al) phase, all of the off-diagonal terms in the diffusivity matrix D_{ij} , where i and j denote i and j components, respectively, are assumed to be zero. The diagonal terms, D_{ii} , are described by the Arrhenius equation:

$$D = D_0 \exp[-Q \times (RT)^{-1}] \quad (3)$$

where D_0 is denoted as the pre-exponential factor and Q as the activation energy. T denotes the absolute temperature, and R the gas constant. The parameters D_0 and Q are usually evaluated from the measurements of diffusion coefficients at a series of temperatures.

Diffusion in the liquid is assumed to be so rapid that the liquid concentration is essentially uniform. The impurity diffusivities in liquid Al, which are needed for the micromodel calculation, are described by an equation similar to Eq. (3).

The dendrite tip undercooling consists of five different contributions [39]: kinetic undercooling, undercooling due to solute trapping, temperature gradient undercooling, solutal undercooling, and undercooling due to the curvature of the tip. In the present experiment, only the solutal undercooling and temperature gradient undercooling play an important role.

Dendrite arm coarsening is calculated in accordance with Beaverstock’s model [42], which is an extension over that by Roósz and Exner [43]. The model of Beaverstock is preferable since it takes into account all solute elements for the calculation of the overall coarsening rate and does not assume that the element with the lowest coarsening rate determines the overall coarsening rate.

An additional extension to the model used by Kraft et al. [39] is that back diffusion in the (Al) phase is considered during the entire solidification process by using the approach of Chen and Chang [44]. Since back diffusion in the solid, dendrite arm coarsening, and undercooling effects are considered only at the solidification stage in which the primary (Al) is solidified [7, 36], the micromodel calculation is performed only in this solidification range. When the liquid reaches the region where two or more solid phases solidify simultaneously, the assumptions for the Gulliver–Scheil model are employed, with the exception that the solid-state back diffusion in (Al) is considered.

In addition to the diffusivities [45] in the liquid and (Al) phases, the kinetic data [2, 46] needed in the micromodel calculation are listed in Table 1. The micromodel presented in the present work is coupled with a robust, user-friendly multicomponent phase diagram calculation pro-

Table 1. Kinetic data used for the microstructure and microsegregation modeling of the Al 356.1 and Al 356.2 alloys in directional solidification.^a

Impurity diffusivity of Fe in liquid Al	$D_{\text{Fe}}^{\text{L-Al}} = 2.34 \times 10^{-7} \exp(-4210/T) \text{ m}^2 \text{ s}^{-1}$	[45]
Impurity diffusivity of Fe in solid (Al)	$D_{\text{Fe}}^{\text{fcc-Al}} = 3.62 \times 10^{-1} \exp(-25738/T) \text{ m}^2 \text{ s}^{-1}$	[45]
Impurity diffusivity of Mg in liquid Al	$D_{\text{Mg}}^{\text{L-Al}} = 9.90 \times 10^{-5} \exp(-8612/T) \text{ m}^2 \text{ s}^{-1}$	[45]
Impurity diffusivity of Mg in solid (Al)	$D_{\text{Mg}}^{\text{fcc-Al}} = 1.49 \times 10^{-5} \exp(-14493/T) \text{ m}^2 \text{ s}^{-1}$	[45]
Impurity diffusivity of Mn in liquid Al	$D_{\text{Mn}}^{\text{L-Al}} = 1.93 \times 10^{-7} \exp(-3728/T) \text{ m}^2 \text{ s}^{-1}$	[45]
Impurity diffusivity of Mn in solid (Al)	$D_{\text{Mn}}^{\text{fcc-Al}} = 1.35 \times 10^{-2} \exp(-25438/T) \text{ m}^2 \text{ s}^{-1}$	[45]
Impurity diffusivity of Si in liquid Al	$D_{\text{Si}}^{\text{L-Al}} = 1.34 \times 10^{-7} \exp(-3608/T) \text{ m}^2 \text{ s}^{-1}$	[45]
Impurity diffusivity of Si in solid (Al)	$D_{\text{Si}}^{\text{fcc-Al}} = 1.38 \times 10^{-5} \exp(-14144/T) \text{ m}^2 \text{ s}^{-1}$	[45]
Energy of solid/liquid interface	$\gamma = 0.093 \text{ J m}^{-2}$	[2]
Specific latent heat of solidification	$\Delta h = 9.5 \times 10^8 \text{ J m}^{-3}$	[46]
Geometric factor for coarsening	$G = 35 \text{ J m}^{-3}$	[2]

^a Alloy 356.1: 91.95 wt.% Al–0.46 wt.% Fe–0.3 wt.% Mg–0.32 wt.% Mn–6.97 wt.% Si
Alloy 356.2: 92.77 wt.% Al–0.08 wt.% Fe–0.35 wt.% Mg–6.8 wt.% Si

Table 2. Comparison of the calculated and measured invariant reaction temperatures for Al-rich parts of the Al–Fe–Mg, Al–Fe–Mn, and Al–Mg–Mn systems.

System	Reaction	Measured T (°C)	Calculated T (°C)
Al–Fe–Mg	$\text{L} \rightleftharpoons (\text{Al}) + \text{Al}_{13}\text{Fe}_4 + \text{Al}_8\text{Mg}_5$	451 [16]	450 (this work)
Al–Fe–Mn	$\text{L} + \text{Al}_{13}\text{Fe}_4 + \text{Al}_6\text{Mn} \rightleftharpoons \text{Al}_6\text{Mn}$	730 [17]	750 (this work)
	$\text{L} \rightleftharpoons (\text{Al}) + \text{Al}_{13}\text{Fe}_4 + \text{Al}_6\text{Mn}$	654 [16]	654 (this work)
Al–Mg–Mn	$\text{L} \rightleftharpoons (\text{Al}) + \text{Al}_6\text{Mn} + \text{Al}_8\text{Mg}_5$	437 [16]	437 (this work)

Table 3. Comparison between the calculated and measured reaction temperatures and liquid compositions for the invariant equilibria in Al-rich corner of the quaternary Al–Fe–Mg–Si system.

Source	Liquid composition (wt.% Fe, wt.% Mg, wt.% Si)	T (°C)
Calculated (this work)	$L + \text{Mg}_2\text{Si} + \beta\text{-AlFeSi} \rightleftharpoons (\text{Al}) + \text{Al}_{18}\text{Fe}_2\text{Mg}_7\text{Si}_{10}$	
Measured [18]	0.60, 5.39, 11.29	570
Calculated [15]	0.55, 6.00, 11.40	568
	0.29, 7.75, 6.910	568
Calculated (this work)	$L + \beta\text{-AlFeSi} \rightleftharpoons (\text{Al}) + (\text{Si}) + \text{Al}_{18}\text{Fe}_2\text{Mg}_7\text{Si}_{10}$	
Measured [18]	0.50, 3.79, 13.40	560
Calculated [15]	0.52, 2.90, 12.15	567
	0.09, 5.52, 13.17	559
Calculated (this work)	$L \rightleftharpoons (\text{Al}) + (\text{Si}) + \text{Mg}_2\text{Si} + \text{Al}_{18}\text{Fe}_2\text{Mg}_7\text{Si}_{10}$	
Measured [18]	0.22, 4.79, 13.62	557
Calculated [15]	0.15, 4.90, 12.90	555
	0.86, 7.44, 18.83	556
Calculated (this work)	$L \rightleftharpoons (\text{Al}) + \text{Mg}_2\text{Si} + \text{Al}_{13}\text{Fe}_4 + \text{Al}_8\text{Mg}_5$	
Measured [19]	0.005, 33.92, 0.095	450
Calculated [15]	0.0001, 33.90, 0.092	447
		451

gram-PanEngine [47] to carry out prediction for microstructure and microsegregation. PanEngine utilizes the established thermodynamic database in order to provide phase equilibrium information on the solid/liquid interface.

5. Results and discussions

5.1. Thermodynamic calculation

The thermodynamic optimization was performed by means of the PARROT program [48], and the thermodynamic calculation was carried out with PanEngine [47]. In order to reproduce the experimentally measured phase equilibria on the Al-rich sides of the Al–Fe–Mg, Al–Fe–Mn, and Al–Mg–Mn systems [16, 17], the regular interaction parameters for the liquid phase of the above three ternary systems

are adjusted. The assessed regular parameters are ${}^{\circ}L_{\text{Al,Fe,Mg}}^{\text{L}} = -100 \text{ kJ}/(\text{mol-atoms})$, ${}^{\circ}L_{\text{Al,Fe,Mn}}^{\text{L}} = -200 \text{ kJ}/(\text{mol-atoms})$, and ${}^{\circ}L_{\text{Al,Mg,Mn}}^{\text{L}} = -220 \text{ kJ}/(\text{mol-atoms})$. Table 2 compares the calculated and observed invariant equilibria in Al-rich regions of the ternary systems, showing a good agreement.

As indicated in the preceding section, it is of interest to reassess the Al–Fe–Mg–Si quaternary system. In the present work, the Gibbs energy of formation for the quaternary phase $\text{Al}_{18}\text{Fe}_2\text{Mg}_7\text{Si}_{10}$ relative to its constituent elements is optimized to be $-12027 \text{ J}/(\text{mol-atoms})$ by using the measured invariant phase equilibria [18, 19]. The thermodynamic properties for the pure elements are taken from the compilation of Dinsdale [49]. The calculated phase equilibria agree reasonably with the experimental data [18, 19], as shown in Table 3 and Fig. 1.

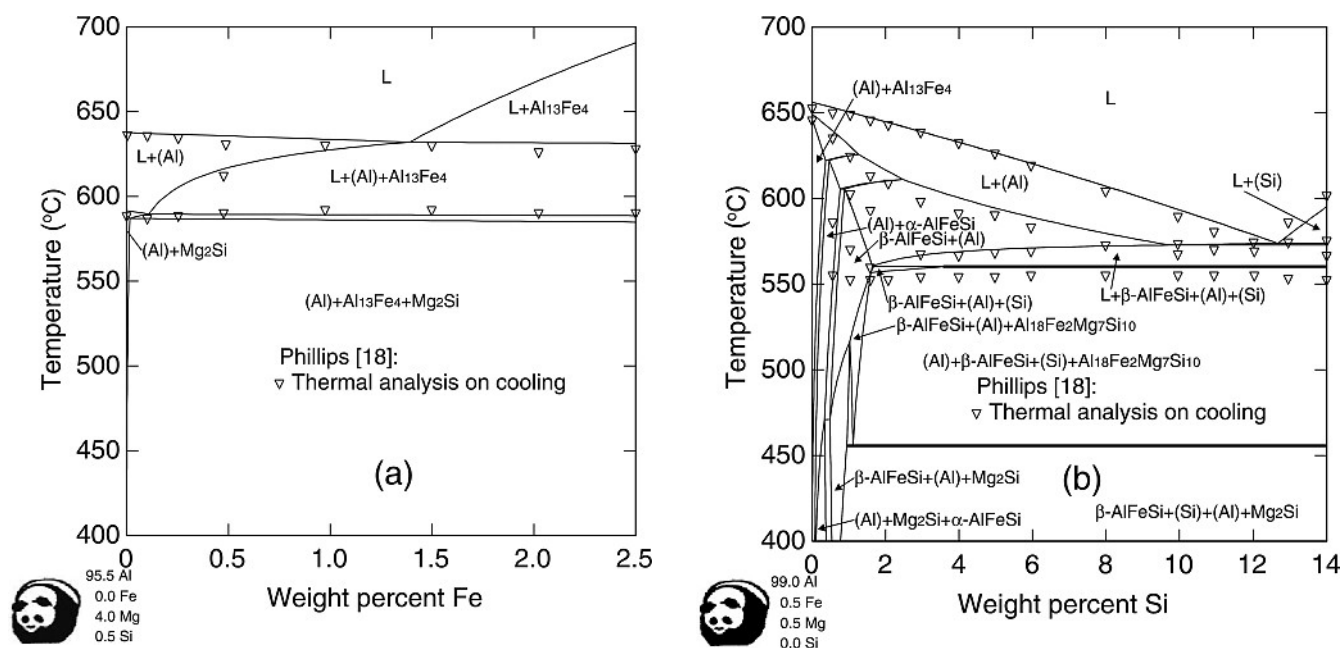


Fig. 1. Calculated isopleths in the Al–Fe–Mg–Si system along with the experimental data from Phillips [18]. (a) 4 wt.% Mg and 0.5 wt.% Si and (b) 0.5 wt.% Mg and 0.5 wt.% Fe.

Table 4 lists the optimized thermodynamic parameters in the Al–Fe–Mn–Si quaternary system. The computed and observed temperatures and the liquid compositions for the invariant reactions are presented in Table 5, showing reasonable agreement for most of the reactions. Small discrepancies exist between the computed and measured invariant reaction temperatures for $L + Al_{13}Fe_4 + Al_4Mn \rightleftharpoons Al_6Mn + \beta-AlMnSi$ and $L + Al_{13}Fe_4 + \beta-AlMnSi \rightleftharpoons \alpha-AlMnSi + Al_6Mn$. These discrepancies are traced to the difference between the calculated (751 °C) [12] and measured (730 °C) [21] temperatures for the reaction $L + Al_{13}Fe_4 + Al_4Mn \rightleftharpoons Al_6Mn$ in the Al–Fe–Mn ternary system. Figure 2 compares the calculated compositions

for $\alpha-AlMnSi$ and $\beta-AlFeSi$ at 550 °C in the four-phase region ((Al), (Si), $\alpha-AlMnSi$, and $\beta-AlFeSi$) with the measured values from Davignon et al. [31]. The fit to the experimental data is reasonable. All of the measured [31] phase assemblages (i. e., (Al) + (Si) + $\alpha-AlMnSi$ + $\beta-AlFeSi$, (Al) + (Si) + $\alpha-AlMnSi$, (Al) + $\alpha-AlMnSi$, (Al) + $\alpha-AlMnSi$ + $Al_{13}Fe_4$, and (Al) + $Al_{13}Fe_4$ + Al_6Mn) are confirmed by the present modeling. A further check on the reliability of the thermodynamic modeling is provided in Figs. 3 and 4, where the model-predicted liquidus temperatures and one typical isopleth are compared with the corresponding experimental values from Zakharov et al. [25, 26] and Phillips and Varley [21], respectively. It is demon-

Table 4. Summary of the optimized thermodynamic parameters in the Al–Fe–Mn–Si quaternary system.^a

Al₈FeMnSi₂: Model $Al_{16/23}Fe_{2/23}Mn_{2/23}Si_{3/23}$		
${}^{\circ}G_{Al_8FeMnSi_2}^{Tl}$	$-(16/23) {}^{\circ}G_{Al}^{fcc-A1} - (2/23) {}^{\circ}G_{Fe}^{bcc-A2} - (2/23) {}^{\circ}G_{Mn}^{cbcc-A12} - (3/23) {}^{\circ}G_{Si}^{dia}$	$= -17\,236 - 1.09865\,T$
α-AlMnSi: Model $Al_{16/23}(Fe, Mn)_{4/23}Si_{1/23}(Al, Si)_{2/23}$		
${}^{\circ}G_{Al:Fe:Si:Al}^{\alpha-AlMnSi}$	$-(18/23) {}^{\circ}G_{Al}^{fcc-A1} - (4/23) {}^{\circ}G_{Fe}^{bcc-A2} - (1/23) {}^{\circ}G_{Si}^{dia}$	$= -17\,000$
${}^{\circ}G_{Al:Fe:Si:Si}^{\alpha-AlMnSi}$	$-(16/23) {}^{\circ}G_{Al}^{fcc-A1} - (4/23) {}^{\circ}G_{Fe}^{bcc-A2} - (3/23) {}^{\circ}G_{Si}^{dia}$	$= -17\,000$
${}^{\circ}L_{Al:Fe,Mn:Si:Al}^{\alpha-AlMnSi}$	${}^{\circ}L_{Al:Fe,Mn:Si:Si}^{\alpha-AlMnSi}$	$= -12\,551 + 13.58446\,T$
${}^1L_{Al:Fe,Mn:Si:Al}^{\alpha-AlMnSi}$	${}^1L_{Al:Fe,Mn:Si:Si}^{\alpha-AlMnSi}$	$= -11\,035$
β-AlFeSi: Model $Al_{0.598}(Fe, Mn)_{0.152}Si_{0.1}(Al, Si)_{0.15}$		
${}^{\circ}G_{Al:Mn:Si:Al}^{\beta-AlFeSi}$	$-0.748 {}^{\circ}G_{Al}^{fcc-A1} - 0.152 {}^{\circ}G_{Mn}^{cbcc-A12} - 0.1 {}^{\circ}G_{Si}^{dia}$	$= -8\,000$
${}^{\circ}G_{Al:Mn:Si:Si}^{\beta-AlFeSi}$	$-0.598 {}^{\circ}G_{Al}^{fcc-A1} - 0.152 {}^{\circ}G_{Mn}^{cbcc-A12} - 0.25 {}^{\circ}G_{Si}^{dia}$	$= -8\,000$

^a In J/(mole of atom); temperature (T) in Kelvin. The Gibbs energies for the pure elements are from the compilation of Dinsdale [49].

Table 5. Comparison between calculated and measured reaction temperatures and liquid compositions for the invariant equilibria in Al-rich part of the quaternary Al–Fe–Mn–Si system.

Source	Liquid composition (wt.% Fe, wt.% Mn, wt.% Si)	T (°C)
Measured [21]	$L + Al_{13}Fe_4 + Al_4Mn \rightleftharpoons Al_6Mn + \beta-AlMnSi$	731
Calculated (this work)	2.35, 3.85, 0.35 4.01, 6.41, 0.02	746
Measured [21]	$L + Al_{13}Fe_4 + \beta-AlMnSi \rightleftharpoons \alpha-AlMnSi + Al_6Mn$	695
Calculated (this work)	2.35, 2.60, 1.35 2.45, 2.03, 0.20	714
Measured [21]	$L + Al_6Mn \rightleftharpoons (Al) + \alpha-AlMnSi + Al_{13}Fe_4$	648
Calculated (this work)	2.00, 0.35, 1.75 1.64, 0.65, 0.20	645
Measured [24]	$L \rightleftharpoons (Al) + \alpha-AlMnSi + Al_{13}Fe_4 + \alpha-AlFeSi$	< 630
Calculated (this work)	$\approx 2.5, < 0.2, \approx 4$ 2.10, 0.02, 4.01	630
Measured [24]	$L + \alpha-AlFeSi \rightleftharpoons (Al) + \beta-AlFeSi + \alpha-AlFeSi$	≈ 600
Calculated (this work)	$\approx 1.5, \approx 0.3, \approx 7$ 1.75, 0.02, 6.5	616
Measured [21]	$L \rightleftharpoons (Al) + (Si) + \alpha-AlMnSi + \beta-AlFeSi$	575
Calculated (this work)	0.60, 0.20, 11.70 0.70, 0.14, 12.63	574
Measured [25]	$L \rightleftharpoons (Al) + (Si) + Al_8FeMnSi_2$	576
Calculated (this work)	0.36, 0.40, 12.40 0.37, 0.44, 12.64	576
Measured [25]	$L \rightleftharpoons (Al) + (Si) + Al_8FeMnSi_2 + \alpha-AlMnSi$	575
Calculated (this work)	0.17, 0.52, 12.40 0.38, 0.43, 12.64	576

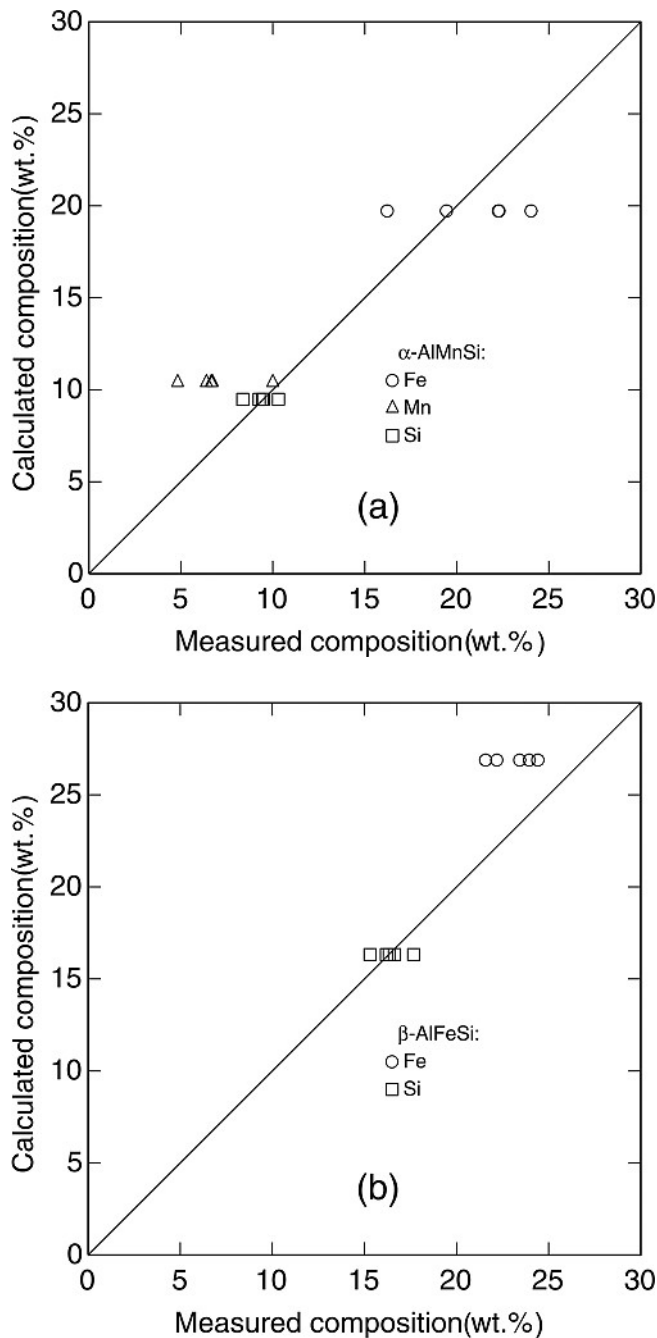


Fig. 2. Calculated compositions for α -AlMnSi and β -AlFeSi in the four-phase equilibrium region ((Al), (Si), α -AlMnSi and β -AlFeSi), compared with the experimental values of Davignon et al. [31]. (a) α -AlMnSi and (b) β -AlFeSi.

strated that the experimental data are reasonably described by the thermodynamic calculation. The calculated liquidus temperature corresponding to the composition of the sample prepared by Flores-Valdes et al. [30] is 815 °C, which is higher by 20 °C than the measured one [30]. According to the present calculation, the quaternary phase $\text{Al}_8\text{FeMnSi}_2$ is formed via a peritectic reaction $\text{L} + \text{Al}_{13}\text{Fe}_4 \rightleftharpoons \text{Al}_8\text{FeMnSi}_2$ at 821 °C.

By using the established thermodynamic database, the computed quinary eutectic temperature for the reaction $\text{L} \rightleftharpoons (\text{Al}) + \text{Al}_3\text{Fe} + \text{Al}_8\text{Mg}_5 + \text{Mg}_2\text{Si} + \text{Al}_8\text{Mg}_2\text{Mn}_2$ is 437 °C, which agrees reasonably with the measured value of 445 °C [24].

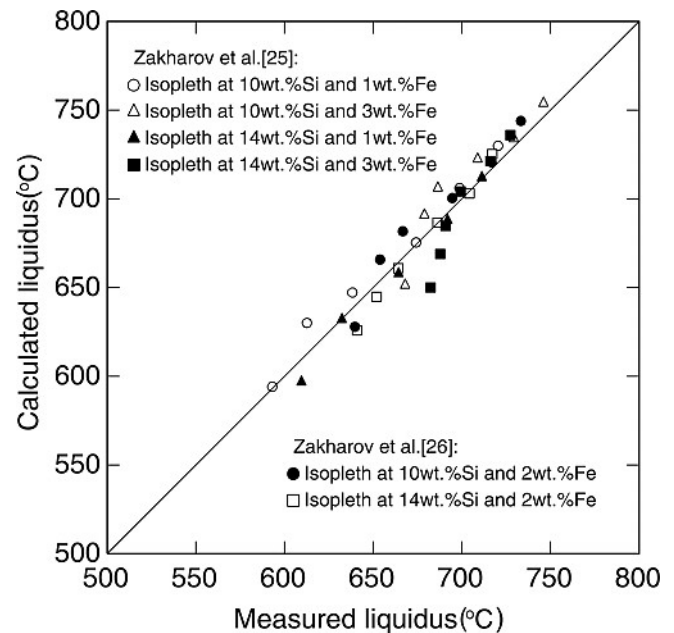


Fig. 3. Calculated liquidus temperatures in the Al–Fe–Mn–Si system with the experimental data from Zakharov et al. [25, 26]. These experimental data are not used in the evaluation of the parameters.

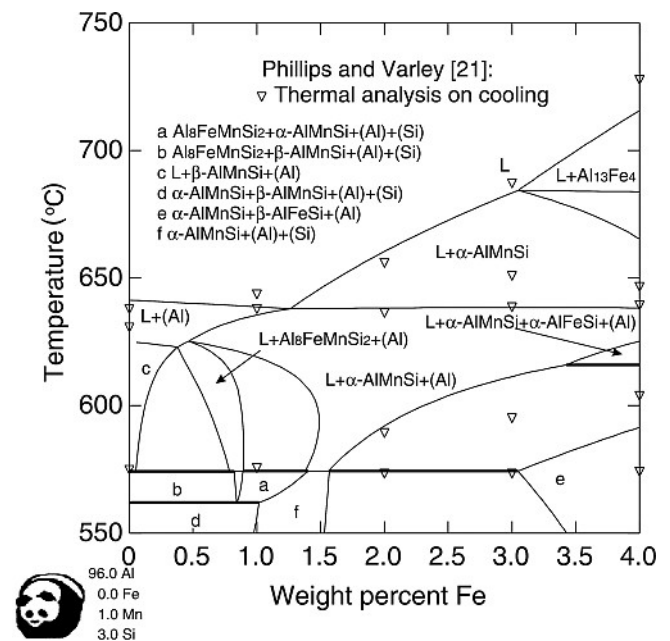


Fig. 4. Calculated isopleth at 1 wt.% Mn and 3 wt.% Si in the Al–Fe–Mn–Si system along with the experimental data from Phillips and Varley [21].

As described in the experimental section, the as-cast Al 356.1 sample is annealed at 500 °C for 45 days in order to reach equilibrium. The water-quenched sample is then subjected to DSC measurement to provide phase transition temperatures under the conditions of equilibrium solidification. The corresponding heat flow versus temperature is shown in Fig. 5. The obtained DSC signals at 575, 586, and 616 °C correspond to the computed reaction temperatures at 573 °C for $\text{L} \rightleftharpoons (\text{Al}) + (\text{Si}) + \beta$ -AlFeSi + α -AlMnSi, at 589 °C for $\text{L} \rightleftharpoons (\text{Al}) + \alpha$ -AlMnSi + β -AlFeSi, and at 615 °C for $\text{L} \rightleftharpoons (\text{Al})$, respectively. This ex-

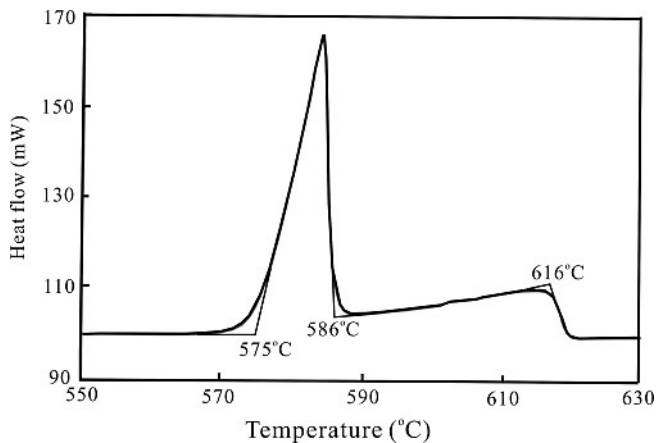


Fig. 5. Heat flow versus temperature for Al356.1 alloy annealed at 500 °C for 45 days. The heating rate is 5 K min⁻¹.

cellent agreement is an additional evidence for the reliability of the presently established thermodynamic database in the Al–Fe–Mg–Mn–Si quinary system.

In the present work, Gulliver–Scheil simulations are also performed to describe the solidification behaviors of Al 356.1 and Al 356.2 alloys. The simulations are conducted in order to further verify reliability of the established Al–Fe–Mg–Mn–Si thermodynamic database. Table 6 compares the microstructure of the solidified alloys according to different sources. As can be seen from this table, the microstructure resulting from the Gulliver–Scheil model is identical to the generally observed one [50]. The microstructure according to equilibrium solidification calculation is, however, different from the observed one. In Table 7, the calculated temperature ranges for solidification are com-

pared with the temperature ranges critically reviewed by Bäckerud et al. [50]. Again, the temperature ranges according to the Gulliver–Scheil model are close to the observed ones. The equilibrium calculation, in which supercooling is not considered, leads to a narrower temperature range than the experimental one. The magnitude of the dimensionless diffusion time (Fourier number) describes the reaction extent resulting from solid–state diffusion. The Fourier number is defined as $\alpha = (D_s \cdot t_f)/L^2$, where D_s is the impurity diffusivity in solid, t_f is the local solidification time, and L is the system size. When α is equal to zero, there is no solid-state diffusion. No information is available on the system size in Ref. [50]. In the present work, the system size is assumed to be 10⁻⁴ m based on the reported dendrite arm spacing [50]. The major species Si in the alloys is used for the calculation of impurity diffusivity in the solid (Al) phase, and the average temperature between liquid temperature and solidification end temperature is utilized in the Arrhenius equation. Using the estimated system size and solid-state diffusivity [45] as well as the solidification time presented in Ref. [50], the estimated Fourier number corresponding to the Al 356.1 alloy with the cooling rate of 0.2 °C/s is about 0.07. The obtained small value of the Fourier number implies that the Gulliver–Scheil model is a good approximation for the experimental conditions reported in Ref. [50].

Tables 8 and 9 list the major reactions during the solidification for the alloys 356.1 and 356.2, respectively. Noticeable discrepancies exist between the equilibrium calculation and experimental observation. The agreement between Gulliver–Scheil simulation and experiment is reasonable. Because of experimental difficulties and the lack of reliable multicomponent phase diagrams, some different

Table 6. Microstructure of Al 356.1 and Al 356.2 alloys obtained on the conditions of different solidification.^a

Solidification condition	Alloy 356.1	Alloy 356.2
Equilibrium solidification	(Al) + (Si) + α -AlMnSi + β -AlFeSi	(Al) + (Si) + β -AlFeSi
Gulliver–Scheil solidification	(Al) + (Si) + α -AlMnSi + β -AlFeSi + Mg ₂ Si + Al ₁₈ Fe ₂ Mg ₇ Si ₁₀	(Al) + (Si) + β -AlFeSi + Mg ₂ Si + Al ₁₈ Fe ₂ Mg ₇ Si ₁₀
Experimentally observed microstructure [50]	(Al) + (Si) + α -AlMnSi + β -AlFeSi + Mg ₂ Si + Al ₁₈ Fe ₂ Mg ₇ Si ₁₀ ^b	(Al) + (Si) + β -AlFeSi + Mg ₂ Si + Al ₁₈ Fe ₂ Mg ₇ Si ₁₀ ^b
Directional solidification with the cooling rate of 2 K/sec (this work)	(Al) + (Si) + α -AlMnSi + β -AlFeSi + Mg ₂ Si	

^a Alloy 356.1: 91.95 wt.% Al–0.46 wt.% Fe–0.3 wt.% Mg–0.32 wt.% Mn–6.97 wt.% Si

Alloy 356.2: 92.77 wt.% Al–0.08 wt.% Fe–0.35 wt.% Mg–6.8 wt.% Si

^b Detected only at high cooling rate.

Table 7. Comparison of ΔT intervals (temperature range for solidification) for Al 356.1 and Al 356.2 alloys under different solidification conditions.^a

ΔT interval (°C) from different sources	Alloy 356.1	Alloy 356.2
Equilibrium solidification	49	52
Gulliver–Scheil solidification	59	60
Experimentally measured ranges [50]	73 ^b	71 ^c

^a Alloy 356.1: 91.95 wt.% Al–0.46 wt.% Fe–0.3 wt.% Mg–0.32 wt.% Mn–6.97 wt.% Si

Alloy 356.2: 92.77 wt.% Al–0.08 wt.% Fe–0.35 wt.% Mg–6.8 wt.% Si

^b Cooling rate of 0.2 °C/s

^c Cooling rate of 0.3 °C/s

Table 8. Calculated major reactions for Al 356.1 alloy under different solidification conditions, compared with the experimental results.^a

Reaction according to Equilibrium solidification	Reaction according to Gulliver–Scheil solidification	Experimentally observed reaction [50]
$L \rightleftharpoons (Al)$ at 615 °C $L \rightleftharpoons (Al) + \alpha\text{-AlMnSi}$ at 589 °C $L \rightleftharpoons (Al) + \alpha\text{-AlMnSi}$ $+ \beta\text{-AlFeSi}$ at 582 °C $L \rightleftharpoons (Al) + (Si) + \beta\text{-AlFeSi}$ $+ \alpha\text{-AlMnSi}$ at 573 °C Solidification is complete.	$L \rightleftharpoons (Al)$ at 615 °C $L \rightleftharpoons (Al) + \alpha\text{-AlMnSi}$ at 588 °C $L \rightleftharpoons (Al) + \alpha\text{-AlMnSi}$ $+ \beta\text{-AlFeSi}$ at 581 °C $L \rightleftharpoons (Al) + (Si) + \beta\text{-AlFeSi}$ $+ \alpha\text{-AlMnSi}$ at 572 °C $L \rightleftharpoons (Al) + (Si) + \beta\text{-AlFeSi}$ $+ \alpha\text{-AlMnSi}$ at 575 °C $L \rightleftharpoons (Al) + (Si) + \beta\text{-AlFeSi}$ $+ \alpha\text{-AlMnSi} + Al_{18}Fe_2Mg_7Si_{10}$ at 559 °C $L \rightleftharpoons (Al) + (Si) + Mg_2Si$ $+ Al_{18}Fe_2Mg_7Si_{10} + \alpha\text{-AlMnSi}$ at 556 °C Solidification is complete	$L \rightleftharpoons (Al)$ at 614 °C $L \rightleftharpoons (Al) + \alpha\text{-AlMnSi}$ at 594 °C $L \rightleftharpoons (Al) + \alpha\text{-AlMnSi}$ $+ \beta\text{-AlFeSi}$ at 594 °C $L \rightleftharpoons (Al) + (Si) + Mg_2Si$ at 555 °C and $L \rightleftharpoons (Al) + (Si) + Mg_2Si$ $+ Al_{18}Fe_2Mg_7Si_{10}$ at 554 °C Solidification is complete

^a Al 356.1 alloy: 91.95 wt.% Al–0.46 wt.% Fe–0.3 wt.% Mg–0.32 wt.% Mn–6.97 wt.% SiTable 9. Calculated major reactions for alloy Al 356.2 under different solidification conditions, compared with the experimental results.^a

Reaction according to Equilibrium solidification	Reaction according to Gulliver–Scheil solidification	Experimentally observed reaction [50]
$L \rightleftharpoons (Al)$ at 616 °C $L \rightleftharpoons (Al) + (Si)$ at 574 °C $L \rightleftharpoons (Al) + (Si) + \beta\text{-AlFeSi}$ at 570 °C $L \rightleftharpoons (Al) + (Si) + \beta\text{-AlFeSi}$ $+ \alpha\text{-AlMnSi}$ at 573 °C Solidification is complete.	$L \rightleftharpoons (Al)$ at 616 °C $L \rightleftharpoons (Al) + (Si)$ at 574 °C $L \rightleftharpoons (Al) + (Si) + \beta\text{-AlFeSi}$ at 568 °C $L + \beta\text{-AlFeSi} \rightleftharpoons (Al) + (Si)$ $+ Al_{18}Fe_2Mg_7Si_{10}$ at 560 °C $L \rightleftharpoons (Al) + (Si) + Mg_2Si$ $+ Al_{18}Fe_2Mg_7Si_{10}$ at 557 °C $L \rightleftharpoons (Al) + (Si) + Mg_2Si$ $+ Al_{18}Fe_2Mg_7Si_{10}$ at 557 °C Solidification is complete.	$L \rightleftharpoons (Al)$ at 615 °C $L \rightleftharpoons (Al) + (Si)$ from 610 to 556 °C $L \rightleftharpoons (Al) + (Si) + \beta\text{-AlFeSi}$ from 610 to 556 °C $L + \beta\text{-AlFeSi} \rightleftharpoons (Al) + (Si)$ $+ Al_{18}Fe_2Mg_7Si_{10}$ at 567 °C $L \rightleftharpoons (Al) + (Si) + Mg_2Si$ at 555 °C $L \rightleftharpoons (Al) + (Si) + Mg_2Si$ $+ Al_{18}Fe_2Mg_7Si_{10}$ at 554 °C Solidification is complete.

^a Al 356.2 alloy: 92.77 wt.% Al–0.08 wt.% Fe–0.35 wt.% Mg–6.8 wt.% Si

reactions are assumed to be of the same temperature in the compilation by Bäckerud et al. [50]. For example, the starting phase transformation temperature for the reactions $L \rightleftharpoons (Al) + \alpha\text{-AlMnSi}$ and $L \rightleftharpoons (Al) + \alpha\text{-AlMnSi} + \beta\text{-AlFeSi}$ in Table 8 is marked to be identical [50]. The present work shows that accurate thermodynamic calculations can provide more detailed information on the phase transitions occurring throughout the solidification.

5.2. Micromodel calculation on microstructure and microstructure

Figure 6 shows the optical microscopy in a transverse section of the alloy 356.1 solidified with a cooling rate of 2 K s^{-1} (a growth rate of $0.04445 \text{ cm s}^{-1} \times$ a temperature gradient of $45 \text{ K cm}^{-1} = 2 \text{ K s}^{-1}$). The composition measurements using EPMA indicate the existence of (Al), $\alpha\text{-AlMnSi}$, $\beta\text{-AlFeSi}$, and (Si). It is worth noting that the measured (Al) phase includes primary (Al) and secondary (Al) since secondary (Al) crystallizes in the binary eutectic

on the surfaces of the primary dendrites and becomes indistinguishable experimentally. (Si) appears in the eutectic-type structures. The two-dimensional element map measurement suggests the existence of trace amount of Mg_2Si phase.

By means of the Gulliver–Scheil model and micromodel, the amounts of the phases solidified throughout the solidification are also calculated, and in Table 10 they are compared with the present experimental data resulting from automatic image analysis of the BSE images. It should be emphasized that the amount of primary (Al) calculated using the Gulliver–Scheil model is only 45 vol.%. As shown in Table 10, the phase fraction of (Al) calculated by using the Gulliver–Scheil model is less than the measured one, while that computed from the micromodel agrees well with the experimental value. According to the Gulliver–Scheil model and micromodel, the amounts of the quaternary phase $Al_{18}Fe_2Mg_7Si_{10}$ are 0.6 and 0.15 vol.%, respectively. In the present experiment, such a trace amount of the phase is not found.

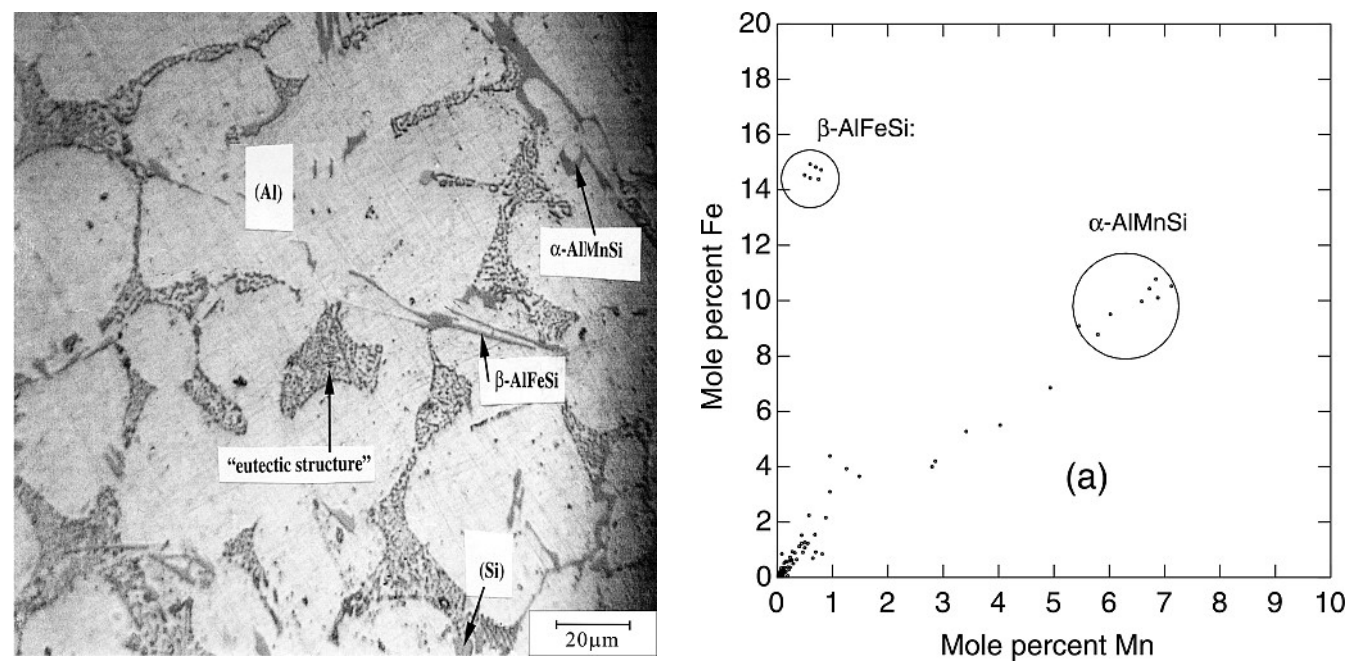


Fig. 6. Optical microstructure in a transverse section of Al 356.1 alloy solidified with a cooling rate of 2 K s⁻¹.

Figure 7a and b show the measured values of the Fe content versus the corresponding values of the Mn content via the area scan approach. It is found that a large part of the points are distributed as a dense cloud at low contents in solutes and are associated with measurements made on the primary (Al) phase. The composition ranges for the primary (Al) could be marked with the square in the diagram. The presently obtained composition ranges for α -AlMnSi and β -AlFeSi phases, which are marked with circles in Fig. 7a, are close to those measured by Davignon et al. [31], confirming the findings of Davignon et al. [31] that β -AlFeSi shows a small solubility for Mn and α -AlMnSi dissolves noticeable amount of Fe. The interaction volume of the EPMA measurement performed in the present work is about 1 μm^2 . The average particle sizes used for EPMA measurement are about 29 μm^2 for (Si), 24 μm^2 for α -AlMnSi, and 44 μm^2 for β -AlFeSi. The estimated maximum uncertainties for composition measurements are about ± 2 at.%. The remaining points are inscribed inside a triangle, the apexes of which are the compositions of (Al), α -AlMnSi and β -AlFeSi. Such points correspond to the measurements made on eutectic-like areas containing at least two of the above three phases.

In order to obtain solute concentration profile in the primary (Al) dendrites as a function of the fractions of the

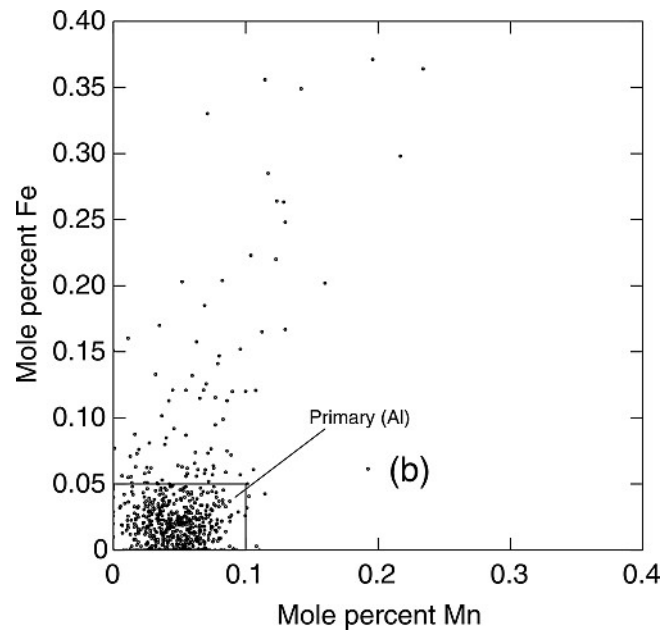


Fig. 7. Experimental correlation between Fe and Mn contents for countings on Al 356.1 alloy solidified with a growth rate of 0.04445 cm s⁻¹ and a temperature gradient of 45 K cm⁻¹ at the liquid-solid interface. (a) in the composition ranges of 0 to 10 at.% Mn and 0 to 20 at.% Fe, and (b) in the composition ranges of 0 to 0.4 at.% Mn and 0 to 0.4 at.% Fe.

Table 10. Amounts of the phases solidified for Al 356.1 alloy from different sources.^a

Source	(Al)	(Si)	α -AlMnSi	β -AlFeSi	Mg ₂ Si	Al ₁₈ Fe ₂ Mg ₇ Si ₁₀
Gulliver–Scheil model	88.0	7.0	1.5	2.5	0.4	0.6
Micromodel	92.75	4.8	0.7	1.4	0.2	0.15
Directional solidification with a cooling rate 2 K/s	93.0	5.1*	0.9	1.0	trace	

^a The amounts of the phases include those solidified throughout the solidification.
* The amount of (Si) is assumed to be 100 minus the sum of (Al), α -AlMnSi and β -AlFeSi.

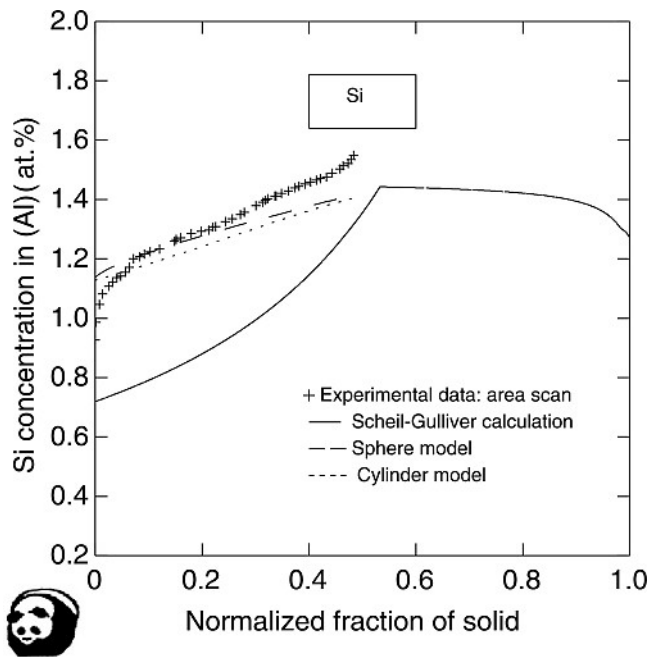


Fig. 8. Si concentration profile in (Al) phase of Al 356.1 alloy. The experimental data are obtained from the directional solidification with a growth rate of $0.04445 \text{ cm s}^{-1}$ and a temperature gradient of 45 K cm^{-1} at the liquid-solid interface.

solid, a mathematic treatment proposed by Flemings et al. [51] and Lacaze and Lesoult [52] was used. The obtained concentration data for a particular component are arranged in increasing or decreasing order. Ordered integer numbers are then assigned to the sorted points, and the integer numbers were normalized linearly to a scale of 0 to 1. Thus obtained fractions are utilized to establish the distribution profiles. The measured and calculated solute distributions of Si corresponding to a cooling rate of 2 K s^{-1} are shown in Fig. 8. Although three geometric shapes are implemented in the present micromodel to describe the growing secondary arms, only two dendrite arm geometries, sphere and cylinder, are employed in the present simulation. The plate geometry is not tested in the present work since it gives rise to the worst agreement with the experimental data among the three geometries [7, 36]. As can be seen from the figure, the calculated concentration profile using the Gulliver–Scheil model [40, 41] is not adequate and significant improvement has been made by means of the micromodel. The measured Mg content is as low as 0.002 mole fractions. It is difficult to obtain accurate experimental data for such a low concentration using EPMA. No comparisons between calculation and measurement are made for Fe and Mn concentration profiles since the measured concentrations are extremely low. Although the solid-state back diffusions in $\alpha\text{-AlMnSi}$ and $\beta\text{-AlFeSi}$ are important because of their noticeable homogeneity ranges, they are not taken into account due to the lack of experimental diffusivities. In (Si) and Mg_2Si phases, the solid-state back diffusion is neglected owing to the small homogeneity ranges.

The second dendrite arm spacing (λ_2) measured from the BSE images is $26 \mu\text{m}$. The calculated λ_2 corresponding to the end of primary (Al) solidification is $19 \mu\text{m}$. It makes sense that the value of λ_2 obtained at the end of primary (Al) solidification is smaller than that resulting from the end of solidification.

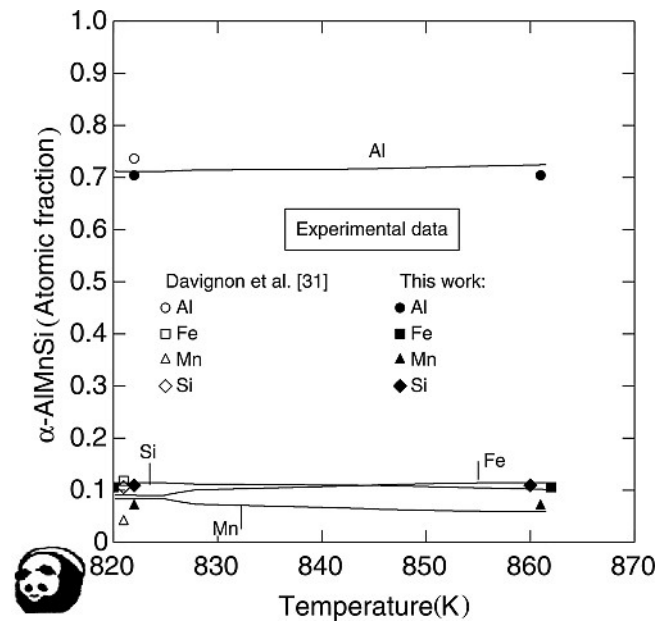


Fig. 9. Calculated solidification path for $\alpha\text{-AlMnSi}$ phase of Al 356.1 alloy according to the micromodel, compared with the equilibrium [31] and non-equilibrium data from the present work.

Finally, the solidification path for $\alpha\text{-AlMnSi}$ is calculated throughout the solidification by means of the micromodel, as shown in Fig. 9. The present average experimental value resulting from eight EPMA point measurements are shown at the start and end states of solidification. Also included is the average composition for $\alpha\text{-AlMnSi}$ at 500°C published by Davignon et al. [31]. The presently measured compositions agree reasonably with the computed values.

6. Conclusions

- The thermodynamic database for the quinary Al–Fe–Mg–Mn–Si system is obtained based on the thermodynamic properties of the edge binary, ternary, and quaternary systems. In particular, the phase equilibria in the Al-rich corner of the quaternary Al–Fe–Mg–Si and Al–Fe–Mn–Si systems are modeled in detail. The reliability of the established database is verified by good agreement between calculation and experiment for phase diagram, equilibrium, and Gulliver–Scheil non-equilibrium solidification behaviors.
- Microstructure and microsegregation in Al 356.1 alloy (91.95Al–0.46Fe–0.3Mg–0.32Mn–6.97Si, in wt.%) are investigated by means of a directional solidification experiment with a growth rate of $0.04445 \text{ cm s}^{-1}$ and a temperature gradient of 45 K cm^{-1} . A quantitative image analysis of backscattered electron micrograph and EPMA area scan approach are utilized to measure the fractions of solids formed and solute redistributions in the primary (Al) phase, respectively. A micromodel is coupled with multicomponent phase diagram calculation to predict the microstructure and microsegregation of the directionally solidified Al 356.1 alloy. Solid-state back diffusion, secondary dendrite arm coarsening, and dendrite tip undercooling are taken into account in the

present micromodel. The calculated results using the micromodel agree reasonably with the experimental data, while the calculation based on the Gulliver–Scheil model deviates noticeably from the experimental observation. The computed secondary dendrite arm coarsening and solidification path using the micromodel are also in good agreement with the experimental values.

We wish to thank Dr. X.Y. Yan for helpful discussion. Thanks are also due to Dr. C. Q. Wang of Advanced Materials Development Center, GM Powertrain, Michigan for providing the cast alloy used in this work. The financial supports from the National Outstanding Youth Science Foundation of China (Grant No. 50425103) and the National Science Foundation of China (Grant No. 50323008) are greatly acknowledged. Y. Du gratefully acknowledges the Furong Chair Professorship program released by Hunan Province of P.R. China for financial support.

References

- [1] J. Lacaze, G. Lesoult, in: J.A. Sekhar, J. Dantzig (Eds.), *Nature and Properties of Semi-Solid Materials*, TMS, Warrendale, Pennsylvania, USA (1991) 105.
- [2] A. Roósz, E. Halder, H.E. Exner: *Mater. Sci. Technol.* 2 (1986) 1149.
- [3] M. Rappaz: *Int. Mater. Rev.* 34 (1989) 93.
- [4] T.P. Battle: *Int. Mater. Rev.* 37 (1992) 249.
- [5] D.M. Stefanescu: *ISIJ Int.* 35 (1995) 637.
- [6] T. Kraft, H.E. Exner: *Z. Metallkd.* 87 (1996) 598.
- [7] F.-Y. Xie, T. Kraft, Y. Zuo, C.-H. Moon, Y.A. Chang: *Acta Mater.* 47 (1999) 489.
- [8] J. Lacaze, G. Lesoult: *ISIJ Int.* 35 (1995) 658.
- [9] T. Kraft: *Z. Metallkd.* 91 (2000) 221.
- [10] U.R. Kattner, W.J. Boettinger, S.R. Coriell: *Z. Metallkd.* 87 (1996) 522.
- [11] B. Meurer, P.J. Spencer, D. Neuschütz: *Z. Metallkd.* 94 (2003) 139.
- [12] I. Ansara, A.T. Dinsdale, M.H. Rand: *COST 507: Thermochemical Database for Light Metal Alloys*, Vol. 2, European Commission, Luxembourg (1998).
- [13] Z.K. Liu, Y.A. Chang: *Metall. Mater. Trans. A* 30 (1999) 1081.
- [14] A. Forsberg, J. Ågren: *J. Phase Equilibria* 14 (1993) 354.
- [15] S.L. Daniel, Ph.D. thesis, University of Wisconsin-Madison, USA (2001).
- [16] P. Villars, A. Prince, H. Okamoto: *Handbook of Ternary Alloy Phase Diagrams*, ASM International, USA (1995).
- [17] W.T. Denholm, J.D. Esdaile, N.G. Siviour, B.W. Wilson: *Metall. Trans. A* 18 (1987) 393.
- [18] H.W.L. Phillips: *J. Inst. Metals* 72 (1946) 151.
- [19] I.T. Gul'din, N.V. Dokukina: *J. Inorg. Chem.* 3 (1958) 359.
- [20] R. Krendelsberger, P. Rogl, A. Leithe-Jasper, C.J. Simensen: *J. Alloys Compd.* 264 (1998) 236.
- [21] H.W.L. Phillips, M.P.C. Varley: *J. Inst. Metals* 69 (1943) 317.
- [22] H. Nowotny, W. Marquardt: *Mikroskopie* 3 (1948) 71.
- [23] G. Phragmen: *J. Inst. Metals* 77 (1950) 489.
- [24] J.G. Barlock, L.F. Mondolfo: *Z. Metallkd.* 66 (1975) 605.
- [25] A.M. Zakharov, I.T. Gul'din, A.A. Arnol'd, Yu.A. Matsenko: *Izv. Vyssh. Uchebn. Zaved., Tsvetn. Metall.* 4 (1988) 89.
- [26] A.M. Zakharov, I.T. Gul'din, A.A. Arnol'd, Yu.A. Matsenko: *Russ. Metall.* 4 (1989) 209.
- [27] H. Thoresen, J.A. Horst, J. Tibballs: *Peritectic precipitation of α -Al (Fe, Mn) Si from the melt*, Senter for Industriforskning, Report N 890222-1, Oslo (1991).
- [28] C. Simensen, T. Rolfsen, J. Tibballs: *Determination of the lattice parameter of α -Al(Fe, Mn)Si crystals*, Senter for Industriforskning, Report N 890222-2, Oslo (1991).
- [29] C. Simensen, A. Bjørnkleit: *Model for α -AlMnSi and α -Al(Fe, Mn)Si*, Senter for Industriforskning, Report N 890222-4, Oslo (1991).
- [30] A. Flores-Valdes, M.I. Pech-Canul, M. Mendez-Nonell, M. Sukiennik: *Scripta Metall.* 30 (1994) 435.
- [31] G. Davignon, A. Sermeels, B. Verlinden, L. Delaey: *Metall. Mater. Trans. A* 27 (1996) 3357.
- [32] Y. Du, J.C. Schuster, F. Weitzer, N. Krendelsberger, B.Y. Huang, Z.P. Jin, W.P. Gong, Z.H. Yuan, H.H. Xu: *Metall. Mater. Trans. A* 35 (2004) 1613.
- [33] A. Flores-Valdes, M. Sukiennik, A.H. Castillejos-E, F.A. Acosta-G, J.C. Escobedo-B: *Intermetallics* 6 (1998) 217.
- [34] B. Onderka, M. Sukiennik, K. Fitzner: *Arch. Metall.* 45 (2000) 119.
- [35] E. Balitshev, T. Jantzen, I. Hurtado, D. Neuschütz: *CALPHAD* 27 (2003) 275.
- [36] X. Yan, S. Chen, F. Xie, Y.A. Chang: *Acta Mater.* 50 (2002) 2199.
- [37] M. Hillert, L.-I. Staffansson: *Acta Chem. Scand.* 24 (1970) 3618.
- [38] B. Sundman, J. Ågren: *J. Phys. Chem. Solids* 24 (1981) 297.
- [39] T. Kraft, M. Rettenmayr, H.E. Exner: *Modelling Simul. Mater. Sci. Eng.* 4 (1996) 161.
- [40] G.H. Gulliver: *J. Inst. Met.* 9 (1913) 120.
- [41] E. Scheil: *Z. Metallkd.* 34 (1942) 70.
- [42] R.C. Beeverstock, in: J. Beech, H. Jones (Eds.), *Solidification Processing 1997*, University of Sheffield, Sheffield, UK (1997) 321.
- [43] A. Roósz, H.E. Exner: *Acta Metall. Mater.* 38 (1990) 375.
- [44] S.-W. Chen, Y.A. Chang: *Metall. Trans. A* 23 (1992) 1038.
- [45] Y. Du, Y.A. Chang, B.Y. Huang, W.P. Gong, Z.P. Jin, H.H. Xu, Z.H. Yuan, Y. Liu, Y.H. He, F.-Y. Xie: *Mater. Sci. Eng. A* 363 (2003) 140.
- [46] W. Kurz, D.J. Fisher: *Fundamentals of Solidification*, 3rd Edition, Trans Tech Publications, Aedermannsdorf, Switzerland (1989).
- [47] S.-L. Chen, S. Daniel, F. Zhang, Y.A. Chang, W.A. Oates, R. Schmid-Fetzer: *PanEngine 1.0-phase equilibrium calculation engine for multicomponent systems*, Madison, Wisconsin, CompuTherm LLC (2000).
- [48] B. Sundman, B. Jansson, J.-O. Andersson: *CALPHAD* 9 (1985) 153.
- [49] A.T. Dinsdale: *CALPHAD* 15 (1991) 317.
- [50] L. Bäckerud, G. Chai, J. Tamminen: *Solidification Characteristics of Aluminum Alloys*, Vol. 2, Foundry Alloys, AFS/Skanaluminium, Sweden (1990).
- [51] M.C. Flemings, D.R. Poirier, R.V. Barone, H.D. Brody: *J. Iron Steel Inst.* 208 (1970) 371.
- [52] J. Lacaze, G. Lesoult: *ISIJ Int.* 35 (1995) 658.

(Received ■; accepted ■)

Correspondence address

Prof. Dr. Yong Du
State Key Laboratory of Powder Metallurgy
Central South University, Changsha, Hunan 410083, P.R. China
Tel.: +86 731 8836 213
Fax: +86 731 8710 855
E-mail: yong-du@mail.csu.edu.cn